Vacuum Nuller Testbed (VNT) Performance, Characterization and Null Control: Progress Report

Richard G. Lyon*[a], Mark Clampin[a], Peter Petrone[b], Udayan Mallik[a], Timothy Madison[a], Matthew
R. Bolcar[a], M. Charley Noecker[c], Stephen Kendrick[c], Michael Helmbrecht[d]

[a]NASA/Goddard Space Flight Center, Greenbelt, MD 20771;
[b]Sigma Space, Lanham MD;
[c]Ball Aerospace and Technology Corp, Boulder CO;
[d]IRIS-AO, Berkeley CA

ABSTRACT

Herein we report on the development, sensing and control and our first results with the Vacuum Nuller Testbed to realize a Visible Nulling Coronagraph (VNC) for exoplanet coronagraphy. The VNC is one of the few approaches that works with filled, segmented and sparse or diluted-aperture telescope systems. It thus spans a range of potential future NASA telescopes and could be flown as a separate instrument on such a future mission. NASA/Goddard Space Flight Center (GSFC) has a well-established effort to develop VNC technologies, and has developed an incremental sequence of VNC testbeds to advance this approach and the enabling technologies associated with it. We discuss the continued development of the vacuum Visible Nulling Coronagraph testbed (VNT). The VNT is an ultra-stable vibration isolated testbed that operates under closed-loop control within a vacuum chamber. It will be used to achieve an incremental sequence of three visible-light nulling milestones with sequentially higher contrasts of 10^8, 10^9 and ideally 10^{10} at an inner working angle of $2*\lambda/D$. The VNT is based on a modified Mach-Zehnder nulling interferometer, with a "W" configuration to accommodate a hex-packed MEMS based deformable mirror, a coherent fiber bundle and achromatic phase shifters. We discuss the initial laboratory results, the optical configuration, critical technologies and the null sensing and control approach.

Keywords: Exosolar planets, visible nulling coronagraph, visible nulling interferometer, coronagraph, wavefront control, null control, interferometry

1. INTRODUCTION

The visible nulling coronagraph (VNC) is an approach to the challenge of direct detection and characterization of exosolar planets. It is currently the only known internal coronagraph approach that works with filled, segmented and sparse or diluted aperture telescope systems [1]. Space telescope system concepts that are based on this approach include: the Extrasolar Planetary Imaging Coronagraph [2,3,4] (EPIC), Diluted Aperture Visible Nulling Coronagraphic Imager [5] (DAViNCI), and, the Advanced Technology for Large Aperture Space Telescope [6] (ATLAST). These were three separate NASA Astrophysics Strategic Mission Concept studies, each of which assessed the feasibility of using a VNC [7,8,9,10] as their prime instrument for exoplanet detection and characterization. The three studies spanned the space of possible aperture configurations of filled, segmented, and diluted/sparse aperture configurations for which the VNC is well suited. The VNC was originally designed and developed for EPIC, but new VNC implementations have been put forth for both ATLAST and DAViNCI [8]. It also lends itself to balloon borne payloads and for ground instruments in both visible and near-infrared (NIR) light.

EPIC would provide insights into the physical nature of a variety of planets in other solar systems complimenting radial velocity (RV) and astrometric planet searches. It would detect and characterize the atmospheres of planets identified by radial velocity surveys, determine orbital inclinations and masses, characterize the atmospheres around A and F stars, and observe the inner spatial structure and colors of inner Spitzer selected debris disks. EPIC would be launched to heliocentric Earth trailing drift-away orbit, with a 5-year mission lifetime. ATLAST and DAViNCI would enable direct detection and characterization of exosolar terrestrial mass planets and characterization of their atmospheres and dust/debris disks.

*Richard.G.Lyon@nasa.gov; phone 1 301 286-4302

Our current approach to the VNC is shown in **Figure-1** and it consists of a modified Mach-Zehnder interferometer with two output ports. It is modified since it has three reflections in each arm as opposed to two in a conventional Mach-Zehnder, and one of the reflections is a specialized custom deformable mirror known as a multiple mirror array (MMA) that consists of hexagonally shaped and hexagonally packed segments. Each segment is articulated in 3 controlled degrees-of-freedoms for piston, tip and tilt. The VNC spatially splits the beam into two separate optical paths at the first beamsplitter (BS) and recombines them with a π phase shift at the second BS. If both beams in each path are identical in amplitude, phase, polarization and wavelength, then due to destructive interference, aka nulling, occurs and no light would exit the output port labeled as science (SCI). Conversely, all of the light would exit at the port labeled bright object sensor (BOS). If the path length difference that is not equivalent to π, then light generally would exit both ports. However, wavefront, amplitude and polarization errors and spectral effects cause light to 'leak' through to the SCI output. The Mach-Zehnder is a symmetric interferometer in that a tip or tilt of the input beam walks the light in the recombined output beams in the same direction, e.g. a Michelson would walk the light in two opposite directions resulting in twin images of the planet.

The VNC is implemented as a coronagraph by introducing an additional phase shift as a function of field angle on the sky. If the path length differences are set such that the phase difference is π on-axis then all light would exit the BOS – thus this would be the starlight. A phase shift of zero, off-axis at the location of the planet, would pass this off-axis light – thus this would be the planet light. The contrast would be the ratio of the two. On-axis leakage would lower the contrast. The field dependent phase shift can be introduced a number of ways but the most straightforward is to shear the beam in one arm of the interferometer relative to the other. A shear of 25% of the pupil diameter results in a piston-like phase difference off-axis that grows linearly with field angle and such that the sine of the piston reaches its 1st maxima at 2 λ/D in angle on the sky. This is generally taken as its inner working angle (IWA), where λ is the wavelength and D is the aperture diameter (or longest baseline for a sparse/dilute system). Thus the goal is to achieve a scientifically-driven contrast (10^9 for Jovian and 10^{10} for terrestrial planets) at the IWA. To mature the VNC as a viable technology and demonstrate null sensing and control to achieve the IWA and contrast traceable to that needed for a flight instrument NASA/GSFC has developed the vacuum nuller testbed (VNT) with the 1st goal of achieving and holding 10^8 contrast at an IWA of 2 λ/D in spectrally narrow (FWHM = 1.2 nm) visible light.

The principle of the VNC has been adequately described elsewhere and the mathematical model of how it operates is well understood see for example, Lyon et. al, 2006, 2008 and the references therein.

Past work has concentrated on proof of principle and we have subsequently demonstrated nulling [9] and the next phase of the VNT efforts are concentrated on quantification of its performance and advancing and refining its control approach to push towards broadband visible nulling approaching the 10^{10} contrast level. Recently the VNT was moved to the new state-of-art lab facilities at GSFC.
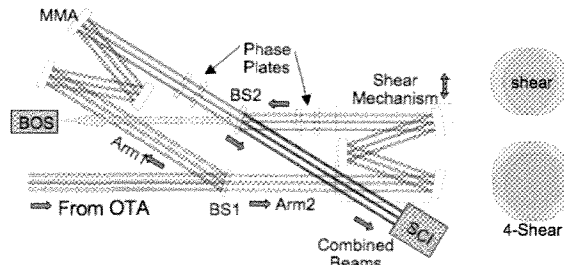

Figure 1 – Schematic of Visible Nulling Coronagraph

2. VACUUM NULLER TESTBED

The VNT has been developed to meet the contrast milestones of 10^8 and 10^9, both narrowband, and at an IWA of 2 λ/D. Additionally we expect to achieve future milestones that are both broader band and higher in contrast. The approach taken is to treat it as a successive process of evaluation, whereby we evaluate the critical technologies, at first separately, then after integration into the testbed and traceable to the science enabling flight requirements of contrast, IWA, spectral bandpass and system stability. The critical technologies include: (i) multiple mirror array (MMA), (ii) spatial filter array (SFA), (iii) null control, and (iv) photon counting detectors and all are at various stages of development with further development expected to continually occur.

2.1 Description of the Visible Nulling Testbed

A top-down photograph of the VNT in its current state is shown in **Figure-2**. The VNT resides on a 24" x 36" optical table. Light enters from a super continuum source outside the vacuum chamber through a single mode fiber at the bottom center of Figure-2. Light exits the single mode optical fiber as approximately as an expanding Gaussian beam into a tubular light trap with black absorbing material. Light can only exit at the left face of the light trap through a 2" apochromatic collimating lens. The lens is stopped down by a circular, black coated, custom metal aperture, to let light
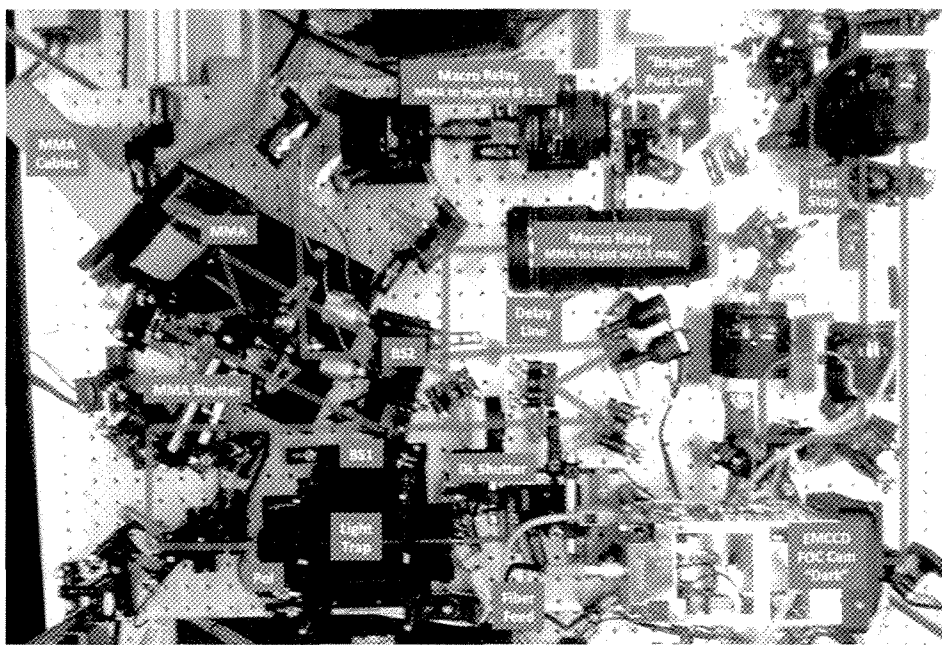
Figure 2 – *Photograph of Visible Nulling Testbed (VNT)*. Optical paths are illustrated in purple. The VNT is on a 36 x 24-inch, 5 inch thick stainless steel platform that can be hoisted into a vacuum tank. Light enters from a source module at bottom center at 'Fiber Feed'. The source module consists of a supercontinuum source with neutral density filters and spectral filters. Light from the source is spatially and spectrally filtered prior to entering the VNT.

exit only over the central 1.6 cm aperture diameter. This effectively forms the aperture stop for the system and allows only ~1/3 of the central diameter of the Gaussian beam to exit insuring a nearly perfect wavefront and amplitude quality, i.e. a high order approximation to a plane wave. A linear polarizer is within the exit port of the light trap with the polarization axis set such that the E-field vector is perpendicular to the plane of Figure-2. This is to insure initially that all reflective optics sees transverse electric (TE) mode fields to minimize polarization cross-leakage. The symmetry of the nuller makes it insensitive to the polarization state of the input field in principle, however differences in coatings, and reflection angles, introduce polarization mismatches. There are two polarizers within the interferometer, one per arm, and two more polarizers, one in front of the two output cameras. Nominally these are all set to the same angle by using a Glan-Thompson prism, and then the two polarizers within the interferometer are rotated such that the light output separately from each arm is matched to within 0.1%. The shutters in each arm are used to accomplish this, as well as monitor the polarization, perform background subtraction and to calculate the contrast. This can be better understood by Equation-1. An output image of the aperture stop on the cameras would yield an image of the form:

$$I(\vec{r}) = I_1(\vec{r}) + I_2(\vec{r}) \pm 2\sqrt{I_1(\vec{r})I_2(\vec{r})}\cos\left[\phi(\vec{r})\right] + B(\vec{r}) + \eta(\vec{r}) \qquad [1]$$

where I_1 and I_2 represent the beams in the two interferometer arms respectively, ϕ represents the difference in phase errors in traversing the interferometer, B is the background and incoherent stray light, η is noise and $\vec{r} = (x, y)$ is the pupil plane coordinate. The $\pm$ is for the bright and dark output channels respectively. Shutting both shutters estimates B and averaging many frames reduces the standard error on B as $\sigma / \sqrt{N}$ where σ is the noise standard deviation and N is the number of frames. In practice N is set to reduce the standard error to less than 1-count of the detector. Opening shutter-1 gives $I_1 + B$ and closing shutter-1 and opening shutter-2 gives $I_2 + B$ and subtracting off the background from each allows for both to be estimated *in-situ* to compensate for source, background, and camera drift. Thus the shutters function as choppers. If instead of operating in the pupil plane, we operate from the focal plane for the dark channel then the shutters still give the I_1 and I_2 terms and the sum of these terms gives the counts without any nulling, i.e. with constructive interference. This is the numerator for the contrast ratio. Thus at each time step both numerator and denominator are estimated and contrast is determined 'on-the-fly'.

After the light trap is an optical relay that images the aperture stop onto the MMA and its counterpart in the other arm of the interferometer, i.e. a real pupil image. There are two custom matched beamsplitters made of high-grade fused silica with dielectric coatings, the first is used to split the beam and the 2nd to recombine. The 1st beamsplitter has its coated side facing the incident light while the 2nd beamsplitter is flipped with the coating side facing in the opposite direction. At the 1st beamsplitter the light is split into a reflective path towards the upper left and a transmissive path towards the right. The transmissive path reflects off three flat optics that are mounted in a "W" configuration. The "W" is aligned such that the input and output beams are parallel and is built and aligned as a separate rigid assembly. This assembly is mounted on a two stage (coarse and fine), 1 degree-of-freedom (DOF) translation stage known as the piston or delay line mechanism. This mechanism is used to change the overall path length in the transmissive arm relative to the reflective arm. The coarse mechanical mechanism is used only at the outset to acquire the white light fringe – white light since a broader spectral filter is initially used insure we locate the central fringe. This alignment is subsequently refined by the fine (piezo) such that the path length differs by < 10 nm at the outset of the closed-loop control. Initially we attempted to actively control the piezo during closed-loop operations but found that using the MMA in closed-loop yields a faster, more precise, and stable control of the path length difference. Following this step the bright channel pupil plane image is used to walk in and indirectly control the wavefront errors by sensing only detector counts over the region of each segment in the pupil image. Conceptually one would want to drive the pupil image bright which yields a dark focal plane image, however it is much less sensitive to drive it bright than to drive it dark, i.e. if one averages the light per MMA segment over each segment and drives the piston, tip and tilt control for each segment to minimize its pupil brightness, then small deviations in the wavefront cause large changes in the averaged light per segment. In practice this camera is limited to a dynamic range of $\sim 10^4$ and this directly limits the sensing and control of the pupil plane null depth. Note that in the pupil domain each segment is independent of each other (control law is diagonal), and thus the algorithm is trivially parallelizable for optimum speed. Once the pupil plane is brought down and held stable the segments are pistoned to realize a π phase shift, making them suddenly appear bright and the dark channels jumps to a much darker state. Control is now is handed off to the dark focal plane. The basic control in the dark focal plane is accomplished by identifying a region of the image that we desire to drive dark and iterating the segment motions with feedback, to minimize the light in this region. In practice the choppers are interlaced throughout to subtract off background and a temporal integrator is used to insure that enough light is available to sense and control within the dark hole - as the hole gets successively darker more frames must be integrated to yield this condition. If an out of spec condition occurs control can step back to the pupil plane. Additionally control can use a weighted form of both the dark and bright channel outputs. During nominal operation there is no wavefront sensing in the classical sense, i.e. only detector counts are collected and piston, tip, tilt error signals are generated to minimize detector counts. Thus the sensing and control does not care whether the errors are from amplitude or phase it only minimizes the detector count which implicitly works to minimize both amplitude and wavefront errors without the need to separate them. This makes the control approach simple and easy to implement. The control aspects of the VNC are very robust and repeatable but the mathematical details will not be described herein as it would take us to far from this descriptive overview.

2.2 Test Configuration

The VNT nominally rests on a 1-Hz air isolation table and is contained within a removable black box. The black box mitigates air turbulence, damps acoustic vibration, and removes unwanted stray light. This configuration serves to facilitate algorithm development and device testing. Subsequently, the VNT is inserted into a vacuum chamber that rests

on passive isolators on the top of the table and the VNT rests on a shelf on top of passive isolators in the vacuum tank. There is an optical feed through on the right wall of the tank and all the electrical feedthroughs are on the left wall of the tank. A water-based chiller system cools the EMCCD camera.

2.3 Description of the Multiple Mirror Array

The reflective arm of the nuller also traverses a "W" configuration towards the upper left, however the first optic is mounted on a shear mechanism. The shear mechanism is a 1-DOF translation stage that translates along the incident beam direction. The effect of this motion, after passing through the "W", is to walk or shear the beam sideways relative to the beam in the nullers other arm. The third optic in this nuller is a microelectricalmechanical (MEMS) deformable mirror with a segmented face sheet known as a multiple mirror array (MMA) as shown in **Figure-3** and described in references [11, 12]. Each of the MMA segments are individually actuated with electrostatic flexure actuators such that each of the segments moves as a rigid body in piston, tip and tilt (3-DOF). The MMAs function is to minimize the wavefront difference between the two arms of the nuller. The MMA operates in closed-loop in conjunction with the piston mechanism, where the mean motion of the aggregate set of MMA segments is integrated and offloaded to the piston mechanism at lower bandwidth of ~1 Hz. This is to keep the MMA from using up its stroke range in compensating for overall piston differences in the two arms of the nuller.
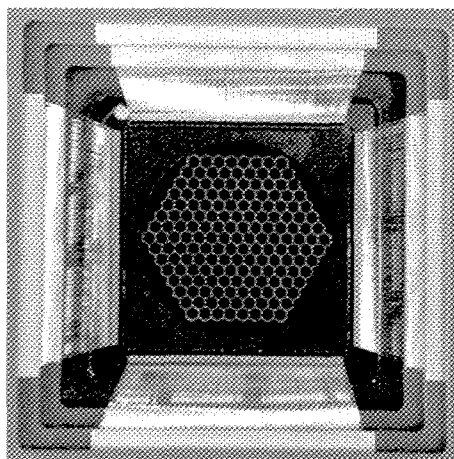

Figure 3 – Photo of an IRIS-AO Multiple Mirror Array (MMA). 169 segments of which 163 are active (outermost 6 inactive). Each segment is ~700 microns point-to-point, gaps are 8 – 10 microns. Full width of active area is ~8.5 mm. Segments are 50-um thick single crystal Si overcoated with protected Al, each moves in 3-DOF. Surface is photographed reflecting black cardboard to accent gap locations.

Both the transmissive and reflective arms of the nuller are combined at the 2nd beamsplitter and yield two output beams known as the bright and dark channels as labeled in Figure-2. Only the dark channel is truly symmetric since it sees the coherent sum of a beam that first reflects off beam splitter 1, and subsequently transmits through beam splitter 2 coherently added to the beam which transmits through beam splitter 1 and reflects of beam splitter 2, i.e.

$$E_D \propto rt + rte^{i\pi} = 0$$

without any wavefront error and where the π phase shift is introduce by the path length difference between the two nuller arms. The bright channel sees a coherent sum of a beam that reflects off both beamsplitters added to a beam that transmits through both beamsplitters, i.e. $E_B \propto r^2 + t^2$ and is thus more sensitive to imbalance in the reflection and transmission of the two beamsplitters. The bright and dark channels pass through two macro lens
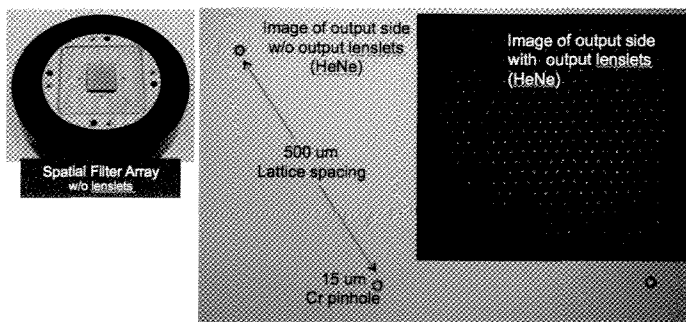

Figure 4: – Spatial Filter Array (SFA) with 217 active fibers; shown w/o lenslets but mounted. Middle – Image of output side without lenslets in HeNe light showing 500 micron lattice spacing. Right - Image of output side with lenslets mounted in HeNe light transmitted through SFA.

groups which for the bright channels relays an image of MMA onto a 16-bit CMOS high frame-rate detector, i.e. a pupil image. The dark channel detector sees a focal plane image on a photon counting cooled E2V camera. All the optics which appear in the non-common path arms of the nuller are high quality flat optics with fused silica substrate and coated with the same broadband coatings except for the MMA and its counterpart in the other arm, both which are coated with protected aluminum from the same coating vendor to balance reflectivities. Additionally the MMA has segment gaps, which are not resident in the other arm of the nuller. The segment gaps introduce Fresnel diffraction effects that are different from the other arm. To correct this problem a high quality optical relay is placed at the output of the VNC after the 2nd beamsplitter. This relay "sees" both the MMA and its counterpart optic in the opposite arm and images them such they are overlaid in the exit pupil (Fig-5 lower left). The aperture of the relay is sufficient to capture the wider angle Fresnel ringing from the free space propagation of the segment gaps resulting in a high quality pupil image. This re-imaged pupil is labeled as Lyot stop in Figure-2; a physical stop is placed at this plane that consists of circular holes laser ablated into titanium foil (Figure-5 lower right) and the foil is coated with highly absorbing black coatings. The holes are 400 microns in diameter while the segments are on a lattice of 613 microns and thus the Lyot stop serves to reduce straylight and to mitigate edge effects on the MMA. The Lyot stop is the exit pupil of the system.

2.4 Description of the Spatial Filter Array

In-between the two-macro lenses of the dark output channel is an assembly for the spatial filter array (SFA). Though not shown explicitly in Figure-2, it is positioned on a special mount that allows it to removed and inserted with minimal realignment, and would be placed where the Lyot is. Initially the SFA will not be used to attain the first milestone of 10^8 contrast. Instead it will tested separately in a second testbed known as the null control breadboard (NCB); a separate white-light Michelson interferometer used for testing the MMA and SFA. The SFA is shown in **Figure-4** and consists of an input lenslet array followed by an array of single mode fibers followed by an output array of lenslets. Each input lenslet is mapped to one fiber and to one output lenslets and each lenslet-fiber-lenslet is optically mapped to one MMA segment. When used passively the SFA cleans up the wavefront errors on the scale of ≥ 1 cycle per MMA segment, since it will be spatially filtered by the fiber. When used in conjunction with the tip/tilt control of the MMA the PSF of a single segment can be steered onto the end of the fiber to lower the coupling efficiency into the fiber. Since the MMA is only in one arm of the VNT, it only affects that component of the beam. If the other arm is slightly darker then mis-steering can be used to balance the amplitude between the beams. Thus the MMA in conjunction with the SFA can in principle control both amplitude and wavefront errors simultaneously. This principle will be validated and its performance assessed.
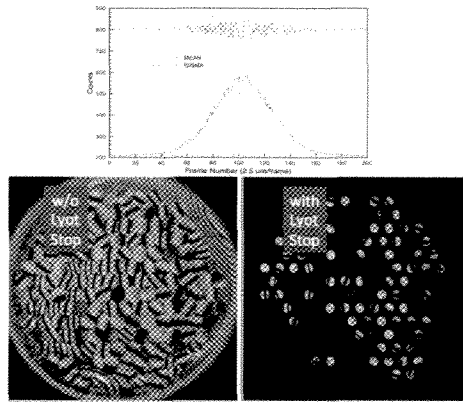
2.5 Null Control and Results

Figure-5: Top – Mean and standard deviation of counts over a MMA segment versus coarse delay line step. Bottom-left Output bright pupil camera image without Lyot stop. Bottom-right Output bright pupil camera image with Lyot stop.
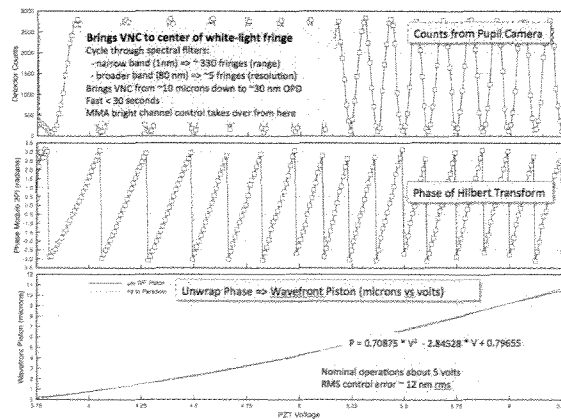

Figure-6: Calibration of Fine Piezo Delay Line. Top – Counts at a single pixel versus delay line voltage. Middle – phase from 1D Hilbert transform. Bottom – unwrapped phase fit to a 2nd order polynomial versus voltage.

The null control refers to sensing and controlling the light and driving it dark to maximize the contrast. It is a misnomer to refer to it as wavefront control since there is no attempt to separate wavefront from amplitude errors. It is critical to be able to optimally sense and control the null, both broad and narrowband, with enough control bandwidth to first achieve, and then hold the contrast, and, to do this repeatedly without levying extreme stability tolerances on the testbed, nor on a flight system. The stroke of the MMAs, bit depth of the cameras, vibration, thermal drift, coating imperfections, temporal and spatial sampling, quantization, flat fielding, dark current, noise, stray light, approximations and errors in the algorithms, along with other potential effects, all work to corrupt this process. The null control is really a multi-step process that consists of a set of camera calibration algorithms, sensing algorithms and delay line-MMA control algorithms. We will not describe herein the mathematical development of the algorithms. However, we will briefly walkthrough the process and show lab results at each step.

Figure-5 shows the initial coarse phasing of the delay line. A broader band spectral filter is inserted. The delay line mechanism is moved in 2.5 micron steps as camera images are collected. The mean and standard deviation versus the motion are

Figure-7: Reachable Space Analysis for MMA

shown at the top of Figure-5. The standard deviation over the region of interference attains a maximum when the fringe visibility is high. This is due to many of the segments having tips and tilts since the MMA is not under control at this time. Thus high visibility implies high standard deviation and no visibility would imply zero standard deviation, since the image would be a uniform grey scale. The coarse delay line is placed at the peak, setting the optical path difference (OPD) to < 10 microns.

The next step in the process is to locate the highest visibility fringe using an even broader filter than coarse delay line. In practice a narrowband filter does not work well since the reduction in the peak of the fringes on either side of the central fringe is not enough, with noise, to guarantee we are on the central fringe. **Figure-6** shows the calibration of the fine delay line versus voltage via a Hilbert transform algorithm.

Figur-8: Demonstration of Bright pupil plane control with 24 MMA Segments

The Hilbert transform (HT) is just the limit as the number of samples tends to infinity for a 4- or 5-bucket type algorithm. The HT is realized by (1) collecting a series of fringe
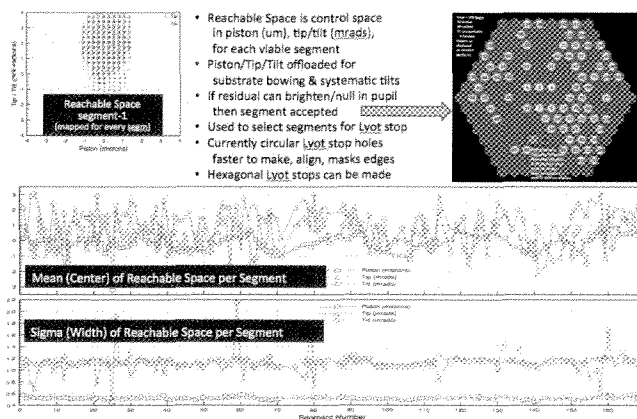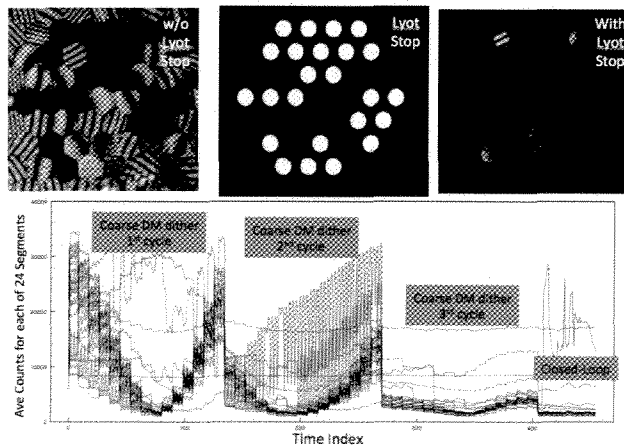
counts versus delay for many fringes (Figure-6 top), (2) 1D Fourier transforming, (3) multiplying the negative frequencies by $-i$ and the positive by $+i$, and (4) inverse transforming. Subsequently taking the arctangent of the ratio of HT to original fringe signal, results in the phase modulo 2π (Fig-6 middle), which is then unwrapped and fit to a polynomial (Fig-6 bottom). This approach is very robust with respect to sampling errors, and low frequency amplitude drift since sampling errors and drift occur common mode in the ratio to the arctangent. In practice we found that hysteresis was a factor if the piezo fine delay was used in closed-loop since it must switch direction, but we worked around this problem by using the MMA piston to offset this effect for fine control. The piezo is nominally used to set the OPD to ~zero +/- 30 nm rms between the two arms of the VNT. Following this, control with the MMA is then initiated.

The next issue is the "reachable space" of the MMA. Reachable space refers to that portion of the piston, tip, tilt space over which a given MMA segment is controllable enough to flatten the MMA, i.e. to compensate for its own substrate bowing and overall wavefront differences between the two arms of the VNT and systematic tip/tilts across the array of MMA segments. Reachable space is mapped by moving each segment in a 3D raster pattern where 3D refers to piston, tip and tilt until the segment walks out of its controllable range, this forms an ellipsoid in piston, tip/tilt space but is not enough to insure that it can be flattened. Thus, once the controllable range is determined, each segment is then controlled within the VNT to null one arm against another to 1 part in 10^4 on the bright pupil camera, i.e. in the pupil plane. If the segment has enough controllable range to reach this criteria then it is designated reachable, otherwise unreachable. Those segments designated unreachable are masked out in the Lyot stop. **Figure-7** shows a graphical representation of this process. Figure-7 upper left shows the ellipsoidal region of reachable space for an individual segment and middle and bottom show the mean (center) and sigma (width) of the reachable space for all the segments, piston is in units of microns of segment motion and tip/tilt is in milli-radians. It was found that for the last MMA delivered from IRIS-AO that about 90 segments were reachable but prior to submission of this manuscript we did not have time to take delivery of a matching Lyot stop for it. We used an older Lyot stop, optimized for a previous delivery of the MMA, but rotated to match as many holes as possible. Those Lyot stop holes that were over unreachable segments we blocked with a silicon based epoxy. This resulted in 44 reachable segments out of a possible 163 segments on the MMA. The next MMA is slated for delivery in October of 2011 and is expected to have a flatter substrate and with 9-fold less systematic tilts, and stronger flexure tips for the piston, tip/tilt actuators mounting points.

Figure-8 shows a demonstration of bright pupil plane camera control with 24 of the segments. Figure-8 top left shows control without the Lyot stop, the middle shows the Lyot stop, and the right shows control with the Lyot stop. The bottom plot shows the initial steps in the control that first attempts to phase all the segments to less than 1-fringe by nutating piston/tip/tilt sequentially. Plotted is the average counts over the region of each segment for all 24 segments. Thus at the far left of this plot versus time the piston nutations occur like a stairstep with the fine ripples for tip and tilt. This obtains a minimum at about 80 steps and stars increasing. The second cycle moves all segments to the minimum but then moves them off to ½ the nutation range of the previous step and this continues through 3 cycles culminating with finer and finer control and ultimately closed-loop where during an integration period the segment piston/tip/tilts stray little from their minima. During this run not all segments achieved a good null as seen as bright segments in the upper right and as the higher plots to the right of the bottom plot.

Figure-9 shows an example of control with 76 segments, not all of which could meet the reachability criteria. However those 44 segments that met the criteria were driven dark to the noise floor of the camera in approximately 200 time steps with 14-bits of MMA control.
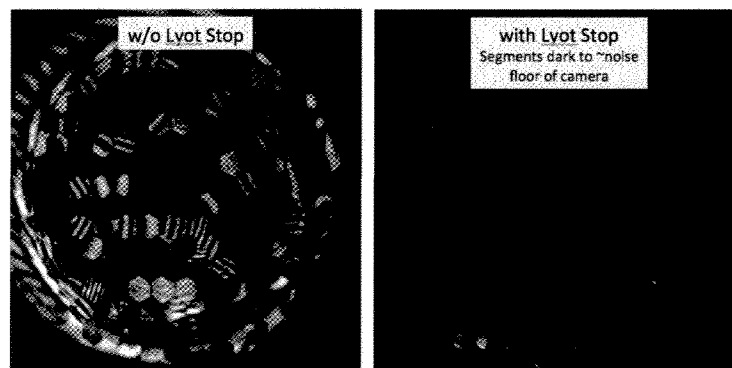
Following this step the

w/o Lyot Stop

with Lyot Stop
Segments dark to ~noise floor of camera

Figure-9: Left – Control of subset of segments without Lyot stop, Right – Control of same subset of segments with Lyot stop. Control is for 200 time steps at 1-Hz with 14-bit control.

44 reachable segments were controlled from the focal plane to generate a dark hole (**Figure-10**). Figure-10 left shows a focal plane image after just at the outset of focal plane control and figure-10 right shows the resultant image after focal plane control. In this level of control each of the controllable segments are iteratively controlled to drive a weighted version of the dark focal plane camera (EMCCD) as dark as possible. The weighted region is shown in the center of the blue circle on right panel of Figure-10. It was found that the larger the selected region the less deep the hole was obtained, however we are still optimizing this control process. We found the dark hole to be repeatable and could be moved in the focal plane within the region of the first set of sidelobes. We fully expect to be able to bring this dark hole down by 2-4 more orders of magnitude by the end of 2011.
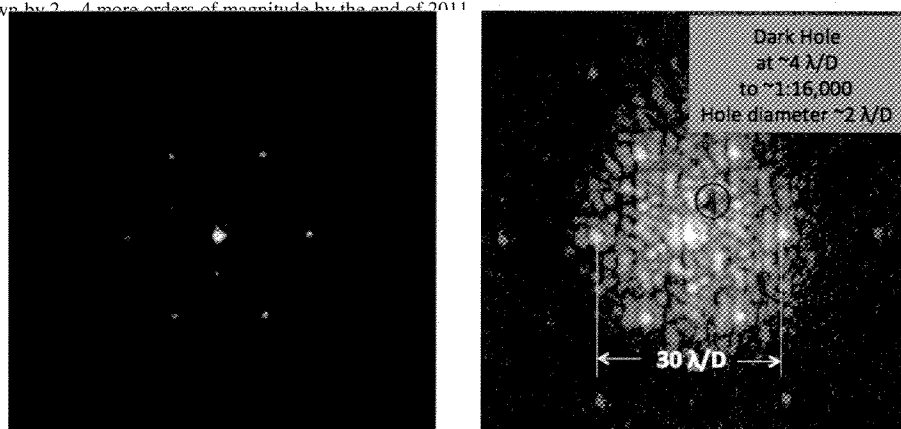

Figure-10: *Example of Focal plane nulling to generate dark Hole.* Hexagonal pattern of sidelobes are due to hex pattern of MMA, 1st sidelobe is at 15 λ/D from the central core. Both images shown on log scale. Left image is after hand-off from pupil plane control, and right image is after control from the dark focal plane to drive the region in blue circle dark.

2.6 Description of Problems and Issues

Two primary problems were addressed as part of this effort: (1) placement of Lyot stops, and (2) MMA reachable space issues.

The Lyot stop placement problem became evident with the initial imaging through the VNT. Initially we desired to place two matched Lyot stops, one at ~2 mm in front of the MMA and the 2nd ~2 mm in front of its counterpart optic in the opposite arm of the VNT. The reasoning for this was based on beam propagation which showed that the aperture stop needn't be imaged onto the DM provided the diffraction occurring in both arms was well matched – this implies that it is not critical for the MMA to be at true pupil image but only within a reasonable depth of focus of the pupil. However placement of the Lyot stops at those locations proved to be difficult since they were both used in double pass, i.e. light 1st transmitted through the Lyot stop holes, reflected off the mirror and passed back through the Lyot stop, and both the MMA and Lyot stop are tilted with respect to the incoming beam at 18 degrees giving a ray retrace error at the Lyot stop edges. The net effect was to introduce effects such as shadowing at the edges. Additionally it required the Lyot stop to be coated to very dark since light reflected and scattered off the front surface coupled back into the nulled beams. We found a simpler and readily achievable solution by placing only a single Lyot at a re-imaged pupil, i.e. we defined the aperture stop to be the entrance pupil and relayed this image onto the MMA, and subsequently relayed this image onto the Lyot stop by using COTS macro zoom lenses. These lenses were used only in common path space, i.e. after the beams were recombined and thus nulling had already occurred and the spectral response of these lenses were not an issue. The main considerations in using these lenses were that they were reasonably well corrected, didn't introduce anamorphic distortion, and that their collection apertures didn't spatially filter the beams to soften or ring the edges of the pupil image at the Lyot stop. These lenses work well and are very forgiving in terms of setting the conjugates and adjusting the plate scale due to their adjustability. However, while suitable for a lab testbed, a flight instrument would replace the lenses with conic mirrors, most likely parabolas, specifically designed to meet the requirements and this implies that there would only be at most two output mirrors for the dark- and two for the bright-channel.

The 2nd issue is that it is believed that existing MMA technology is not currently at the level needed for flight since it is a MEMS based technology that becomes highly reliable and repeatable after many process cycles in the manufacturing process. Since at this time these devices have specialized requirements for coronagraphy not enough of them have been manufactured we believe from any of the known vendors. However, significant advancements have been made with respect to flatter segments, reliability, stiction, coatings, bit depth and controllability. In general our past results with IRIS-AO MMA's have shown them to be promising [10]. While we had some bad and/or unreachable segments on the current MMA the remaining segments were very controlled, had surface flatness of 4 – 6 nm rms, and were very stable and indeed we ultimately use this for fine delay line control also since they have bit level resolution at < 0.1 nm. We are waiting on the next IRIS-AO MMA, expected October 2011, for further testing. However we expect we can meet the milestone with the existing MMA by making a custom Lyot mask that masks out the unreachable segments.

3. SUMMARY

The direct detection and characterization of exosolar planets is a crucial step in the search for habitable planets with liquid water, and potentially life, and addresses the NASA *Search for the Origins of Life* theme. Towards that end we have developed and are in the process of advancing the technologies, for a visible nulling coronagraph approach to coronagraphy via a series of incremental, and well understood, laboratory testbeds. The VNC approach will work with filled, segmented and sparse/dilute aperture telescope systems and thus covers the span of possible future telescope architectures. Additionally it makes maximal use of the output photons since the flux from the target star is conserved from the bright and dark output ports of the VNC. This conservation law in principle gives a robust null control approach that is independent of the state of instrument. Thus as the signal is driven darker the VNC does require increasingly longer integration times to obtain enough photons to sense and control. This implies a fixed control bandwidth for a given target star and is limited only by the brightness of the dimmest target star. Additionally it does not levy beyond state of the art stability requirements on the telescope since the telescope must be stable over each integration window for null control.

REFERENCES

[1] R. G. Lyon, M. Clampin, R. W. Woodruff, G. Vasudevan, P. Thompson, A. Chen, P. Petrone, A. Booth, T. Madison, M. Bolcar, M. C. Noecker, S. Kendrick, G. Melnick, V. Tolls, "Visible Nulling Coronagraphy Testbed Development for Exoplanet Detection", Proceedings of SPIE 7731, San Diego CA (2010)

[2] M. Clampin , R. G. Lyon, G. Melnick, P. Nisenson, R. A. Woodruff, M. Harwit, D.Y. Gezari, L. Petro, H. Ford, R. Mauk, H. Smith, "The Extra-solar Planetary Imaging Coronagraph", Proceedings of SPIE 5487, Glasgow Scotland, June 21 – 25 (2004).

[3] M. Clampin, G. Melnick, R. Lyon, S. Kenyon, D. Sasselov V. Tolls, H. Ford, D. Golimowski, L. Petro, G. Hartig, W. Sparks, G. Illingworth, D. Lin, S. Seager, A. Weinberger, M. Harwit, M. Marley, J. Schneider, M. Shao, M. Levine J. Ge, R. Woodruff, "Extrasolar Planetary Imaging Coronagraph (EPIC)", Proceedings of SPIE 6265, Orlando FL, May (2006).

[4] M. Clampin , R. G. Lyon, G. Melnick, V. Tolls, M. Shao, M. Levine, , R. A. Woodruff, G. Vasudevan, S. Kendrick, "The Extra-solar Planetary Imaging Coronagraph", Mission for Exoplanets Workshop, Pasadena CA, April 21-23, (2009).

[5] Shao, M., Bairstow, S. H., Deems, E., Fletcher, L., Levine, B., Orton, G., Vasisht, G., Wayne, L., Zhao, F., Clampin, M., Lyon, R., Guyon, O., Lane, B., Havey, K., Wynn, J. Samuele, R., Vasudevan, G., Woodruff, R., Tolls, V. Malbet, F., Leger, A., "A Mission Concept Study of a Dilute Aperture Visible Nulling Coronagraph Imager (DAViNCI) for the Detection and Spectroscopy of Exo-planets," BAAS #214, (2009).

[6] Postman, M., "The Science Cases for an Advanced Technology Large-Aperture Space Telescope (ATLAST)," BAAS #215, (2010).

[7] R. G. Lyon, M. Clampin, R. Woodruff, G. Vasudevan, M. Shao, M. Levine, G. Melnick, V. Tolls, P. Petrone, P. Dogoda, J. Duval, J. Ge, "Visible Nulling Coronagraphy for Exo-Planetary Detection and Characterization", IAU Colloquim 200, Direct Imaging of Exoplanets: Science and Technology, Villefranche-sur-Mer, France, (2006).

[8] R. G. Lyon, M. Clampin, G. Melnick, V. Tolls, R. Woodruff, G. Vasudevan, "Extrasolar Planetary Imaging Coronagraph (EPIC): Visible Nulling Coronagraph Testbed Results", Proceedings of SPIE 7010, Marseille Fr, (2008).

[9] R. A. Woodruff, M. Shao, B. Martin Levine, R. Lyon, G. Vasudevan, J. Acu, K. Havey, J. Wynn, "Optical Design of Dilute Aperture Visible Nulling Corongraph Imager," Proc of SPIE 7731, (2010).

[10] R. G. Lyon, M. Clampin, R. Woodruff, G. Vasudevan, P. Thompson, P. Petrone, T. Madison, M. Rizzo, G. Melnick, V. Tolls, "Visible Nulling Coronagraph Testbed Results," Proc of SPIE 7440 (2009).

[11] M. A. Helmbrecht, T. Juneau, M. Hart, and N. Doble, "Performance of a High-Stroke, Segmented MEMS Deformable-Mirror Technology," Invited Presentation, Proc. of SPIE, Vol. 6113, San Jose, CA, Jan. 2006.

[12] M. A. Helmbrecht, M. He, T. Juneau, M. Hart, N. P. Doble, "Segmented MEMS Deformable-Mirror for Wavefront Correction," Invited Presentation, Proc. of SPIE, Vol. 6376, Boston, MA, Oct. 2006.